Radio Science

RESEARCH ARTICLE
10.1029/2019RS006943

Modeling ELF Electromagnetic Field in the Upper Ionosphere From Power Transmission Lines

E. N. Fedorov[1], N. G. Mazur[1], V. A. Pilipenko[2,3], and V. V. Vakhnina[4]

[1]Institute of Physics of the Earth, Moscow, Russia, [2]Geophysical Center, Moscow, Russia, [3]Space Research Institute, Moscow, Russia, [4]Department of Electrotechnics, Togliatti State University, Tolyatti, Russia

Key Points:
- We modeled electromagnetic field in the atmosphere and ionosphere excited by an oscillating 50/100 Hz linear current above the ground
- Leakage rate of power line emission into the upper ionosphere increases during nighttime and above high-resistive crust
- Amplitudes of electromagnetic power line emission detected by LEO satellites correspond to unbalanced line current of about 1 A

Correspondence to:
V. A. Pilipenko,
space.soliton@gmail.com

Citation:
Fedorov, E. N., Mazur, N. G., Pilipenko, V. A., & Vakhnina, V. V. (2020). Modeling ELF electromagnetic field in the upper ionosphere from power transmission lines. *Radio Science*, *55*, e2019RS006943. https://doi.org/10.1029/2019RS006943

Received 13 AUG 2019
Accepted 16 MAY 2020
Accepted article online 29 JUN 2020

Abstract The expected magnitude of extralow-frequency (ELF) electromagnetic response in the upper ionosphere to ground large-scale power transmission lines at low Earth orbit (LEO) is modeled. The full-wave system of Maxwell's equations is numerically solved in a realistic ionosphere whose parameters have been reconstructed with the use of the International Reference Ionosphere (IRI) model. We have calculated the altitudinal structure in the atmosphere and ionosphere of electromagnetic field and Poynting flux excited by an oscillating 50/150 Hz linear current suspended above the ground. The leakage rate into the upper ionosphere was shown to increase during nighttime hours and above a high-resistive crust. The amplitudes of electromagnetic power line emission (PLE) detected by LEO satellites correspond to the unbalanced power line current intensity of about 1–10 A, depending on the crust resistivity.

1. Introduction: Electric Power Lines as Large-Scale ELF Transmitters

The electromagnetic response of the ionosphere to natural and man-made electromagnetic disturbances in the atmosphere (e.g., lightning) and on the ground (e.g., radio transmitters) has been thoroughly studied in the very low frequency (VLF) frequency range (≥1 kHz). Any noticeable radiation efficiency in the VLF range and lower may be expected only for a very large emitting system. Such man-made large-scale transmitters do exist—they are networks of electric power transmission 50/60 Hz lines extended to many hundreds of kilometers (Helliwell et al., 1975).

All industrial power systems with a nonlinear current-voltage response produce a nonsinusoidal current even under normal maintenance conditions and thus generate in a power line high harmonics of the transmitting current. Moreover, a power line for frequencies of 2–8 kHz in fact operates as an effective traveling-wave antenna (Barnett, 1974; Bewley, 1942; Kostrov et al., 2017). As a result, power line harmonic radiation (PLHR), which refers to electromagnetic emissions in the VLF band (from hundreds of hertz to few kilohertz) at equidistant frequencies of 50/60 Hz, can effectively penetrate into the ionosphere and magnetosphere and be detected by satellite's sensors. The PLHR was thoroughly studied both observationally (Bullough et al., 1985; Rothkaehl & Parrot, 2005) and theoretically (Ando et al., 2002; Wu et al., 2014, 2019).

The Low-Earth-orbit (LEO) DEMETER satellite recorded in ~5% of data the PLHR, whereas the occurrence rate of these emissions increased with the Kp index and became higher during nighttime (Nemec et al., 2006). The From OGO-3 data Luette et al. (1979) found evidence that PLHR leaks into the magnetosphere with sufficient intensity to control the starting frequencies of VLF chorus emissions. VLF radiation from electrical power transmission lines was found to stimulate nonlinear wave-particle and wave-wave interactions in the magnetosphere, resulting in growth and triggering of natural chorus emissions (Park & Helliwell, 1981). These results indicated that man-made VLF emissions are an important factor in the generation of chorus, a wave activity that plays a key role in magnetospheric electron acceleration to relativistic energies (Shprits et al., 2008). It was even suggested that PLHR at latitudes of highly industrialized regions may partially deplete the outer radiation belt (Tatnall et al., 1983).

Much less attention was paid to the atmosphere-ionosphere coupling in the extralow-frequency (ELF) range, about several tens to hundreds of hertz, though the 50/60 Hz power line emission (PLE) is one of the most ubiquitous forms of electromagnetic radiation emanating from the Earth. Most of the emitted energy is expected to propagate to large distances in the waveguide formed by the Earth's surface and the bottom edge of the ionosphere (~60–80 km). For example, 60 Hz signals resulting from the United States-Canada electric power systems were reliably recorded in Antarctica (Koloskov & Yampolski,

2009). Given that power lines are widespread, the leakage into the ionosphere of these man-made ELF emissions might be expected in the same manner in which a small fraction of the power associated with Schumann resonances (Simoes et al., 2012) or submarine communication transmitters (Pilipenko et al., 2019) has been found to penetrate into the upper ionosphere. Despite their known frequency signatures and source locations, a direct detection in space of 50/60 Hz emissions associated with terrestrial power lines is not very common. Ionospheric PLEs were discovered in early LEO satellite missions. The search for PLE at OHZORA satellite (350–860 km) was made by recording the intensity of 50 and 60 Hz narrow bands (Tomizawa & Yoshino, 1985). The relative enhancement of 60 Hz magnetic noise in respect to background ELF hiss at 55 Hz was observed over a wide area above industrialized regions of Japan, and relative enhancement at 50 Hz was observed over eastern China.

These observational results were confirmed by recent and more advanced space missions (Pfaff et al., 2014). A large volume of observational data on PLE was obtained by the LEO Chibis-M microsatellite equipped with the ELF-VLF electrical sensor (Dudkin et al., 2015; Korepanov et al., 2015). In the DEMETER satellite observations, the recorded PLE power was larger by about an order of magnitude than the intensity of PLHR events (Nemec et al., 2008). However, a rate of the PLE energy leakage into the upper ionosphere has not been adequately modeled so far with a realistic ionospheric model.

In this paper we investigate theoretically the efficiency of the ELF wave excitation in the upper ionosphere at the frequency of 50 Hz and its third harmonic 150 Hz by a near-ground line current using an elaborated numerical model with a realistic ionospheric profile. The amplitudes of electric and magnetic fields in the ionosphere and atmosphere at various altitudes have been numerically calculated for different ionospheric conditions and crust resistivities. The available results of the PLE detection by LEO satellites are compared with the theoretical predictions. Such comparison enables one to estimate a magnitude of the unbalanced current in electric power lines.

2. Modeling Electromagnetic Field of Horizontal Line Current Above a Conducting Ground

2.1. Model and Basic Equations

We use the multilayered horizontally homogeneous model with vertical geomagnetic field $\mathbf{B}_0$ (inclination $I = \pm 90°$), similar to the model presented in Mazur et al. (2018). We use the Cartesian coordinate system with the unit vectors of coordinate axes $\hat{\mathbf{x}}$, $\hat{\mathbf{y}}$, $\hat{\mathbf{z}}$, and the z axis is directed vertically upward. It is supposed that the electromagnetic field is excited by an infinitely long linear current along axis y, situated at altitude h above the Earth's surface. A current oscillates in time with frequency ω and along the power line with the wave vector k_y, namely, $J(t, y) = J_0 \exp(-i\omega t + ik_y y)$. Therefore, the density of the driver current is

$$\mathbf{j}(x, y, z, t) = J_0 \exp(-i\omega t + ik_y y)\delta(x)\delta(z - h)\hat{\mathbf{y}}. \tag{1}$$

In the ionospheric plasma, the tensor of dielectric permeability in the field-aligned coordinate system has the form

$$\varepsilon = \varepsilon_0 \begin{pmatrix} \varepsilon_\perp & ig & 0 \\ -ig & \varepsilon_\perp & 0 \\ 0 & 0 & \varepsilon_\parallel \end{pmatrix}, \tag{2}$$

where the tensor elements are

$$\varepsilon_\perp = 1 - \sum_j \frac{\omega_{pj}^2(\omega + i\nu_j)}{\omega[(\omega + i\nu_j)^2 - \Omega_j^2]}, \quad g = \sum_j \frac{s_j \omega_{pj}^2 \Omega_j}{\omega[(\omega + i\nu_j)^2 - \Omega_j^2]}, \quad \varepsilon_\parallel = 1 - \sum_j \frac{\omega_{pj}^2}{\omega(\omega + i\nu_j)}.$$

Here ε_0 is the free space dielectric permeability, ω_{pj} is the plasma frequency of charged particles with their sort numbered j, $\Omega_j > 0$ is the cyclotron frequency, and ν_j is the effective collisional frequency; the sign $s_j = +1$ for electrons and $s_j = -1$ for ions. The tensor elements are related to local Pedersen σ_P and Hall σ_H conductivities as $\varepsilon_\perp(\omega) = i\sigma_P(\omega)/(\omega\varepsilon_0)$, and $g(\omega) = -\sigma_H(\omega)/(\omega\varepsilon_0)$.

We search the solution of Maxwell's equations for magnetic field $\mathbf{B}(x,y,z,t)$ and electric field $\mathbf{e}(x,y,z,t) \equiv c^{-1}\mathbf{E}$, normalized to the light velocity c, as harmonics $\propto \exp(-i\omega t + ik_y y)$ (the same as the driver current). The spatial structure across the current (x direction) is presented as the Fourier integral over the wave number k_x

$$\mathbf{B}(x,\,y,\,t) = e^{-i\omega t + ik_y y}\int_{-\infty}^{\infty} e^{ik_x x}\mathbf{B}(k_x)dk_x,\ \mathbf{e}(x,\,y,\,t) = e^{-i\omega t + ik_y y}\int_{-\infty}^{\infty} e^{ik_x x}\mathbf{e}(k_x)dk_x.$$

In Maxwell's equations for spatial spectral components $\mathbf{B}(k_x)$, $\mathbf{e}(k_x)$ the harmonic of the density of the external current $\mathbf{j}(k_x)$ is determined by the inverse Fourier transform of Equation 1

$$\mathbf{j}(k_x) = (2\pi)^{-1}\int_{-\infty}^{\infty} e^{-ik_x x}J_0\delta(x)\delta(z-h)\hat{\mathbf{y}}\,dx = (2\pi)^{-1}J_0\delta(z-h)\hat{\mathbf{y}}. \tag{3}$$

Maxwell's equations for horizontal spatial spectral components $\mathbf{B}_\tau(k_x) = (B_x, B_y)$ and $\mathbf{e}_\tau(k_x) = (e_x, e_y)$ with the account for the external current (3) may be presented in the following matrix form:

$$\begin{aligned} &\partial_z\mathbf{B}_\tau - \mathbf{T}^{bb}\mathbf{B}_\tau = \mathbf{T}^{be}\mathbf{e}_\tau + \mu_0(2\pi)^{-1}J_0\delta(z-h)\hat{\mathbf{x}},\\ &\partial_z\mathbf{e}_\tau - \mathbf{T}^{ee}\mathbf{e}_\tau = \mathbf{T}^{eb}\mathbf{B}_\tau. \end{aligned} \tag{4}$$

This system of four ordinary differential equations for horizontal field components has been obtained after the exclusion of the vertical components B_z and e_z from the complete Maxwell's system. This system coincides with the one from Fedorov et al. (2016) in the case of inclination $I = \pm 90°$. For a vertical geomagnetic field the matrices $\mathbf{T}^{bb} = \mathbf{T}^{ee} = 0$, and the matrices $\mathbf{T}^{be}$ and $\mathbf{T}^{eb}$ are as follows:

$$\mathbf{T}^{be} = \frac{i}{k_0}\begin{pmatrix} -k_x k_y \mp ik_0^2 g & k_x^2 - k_0^2\varepsilon_\perp \\ k_0^2\varepsilon_\perp - k_y^2 & k_x k_y \mp ik_0^2 g \end{pmatrix},$$

$$\mathbf{T}^{eb} = ik_0\begin{pmatrix} k_x k_y(k_0^2\varepsilon_\parallel)^{-1} & 1 - k_x^2(k_0^2\varepsilon_\parallel)^{-1} \\ -1 + k_y(k_0^2\varepsilon_\parallel)^{-1} & -k_x k_y(k_0^2\varepsilon_\parallel)^{-1} \end{pmatrix}.$$

Here $k_0 = \omega/c$ is the wave number of a free space, and the plus/minus sign corresponds to the Southern/Northern Hemisphere.

2.2. Boundary Conditions

We have to impose boundary conditions on the ground ($z = 0$) and in the upper ionosphere ($z \to \infty$). We consider the Earth as a homogeneous half-space with conductivity $\sigma_g = \text{const}$. The horizontal electromagnetic components must match the boundary condition at the Earth's surface ($z = 0$):

$$\mathbf{B}_\tau = \overline{\mathbf{Y}}_g\mathbf{e}_\tau. \tag{5}$$

Here the normalized ground admittance matrix $\overline{\mathbf{Y}}_g$ is

$$\overline{\mathbf{Y}}_g = \frac{1}{k^2}\begin{pmatrix} kxk_y(\overline{Y}_g^{(E)} - \overline{Y}_g^{(H)}) & k_x^2\overline{Y}_g^{(H)} + k_y^2\overline{Y}_g^{(E)} \\ -k_x^2\overline{Y}_g^{(E)} - k_y^2\overline{Y}_g^{(H)} & -k_x k_y(\overline{Y}_g^{(E)} - \overline{Y}_g^{(H)}) \end{pmatrix}, \tag{6}$$

where the partial admittances for electric (E) and magnetic (H) modes are $\overline{Y}_g(H) = \sqrt{\varepsilon_g - (k_x/k_0)^2}$, $\overline{Y}_g(E) = \varepsilon_g/\sqrt{\varepsilon_g - (k_x/k_0)^2}$, $\varepsilon_g = \mathrm{Re}\,\varepsilon_g + i\sigma_g(\omega\varepsilon_0)^{-1}$ is the permittivity of the ground, and $k^2 = k_x^2 + k_y^2$. It is important to notice that for frequencies and ground conductivities considered in this paper, the term $\mathrm{Re}\,\varepsilon_g \sim 10$ may be neglected with a very good accuracy.

Also, the emission condition at $z \to \infty$ must be fulfilled:

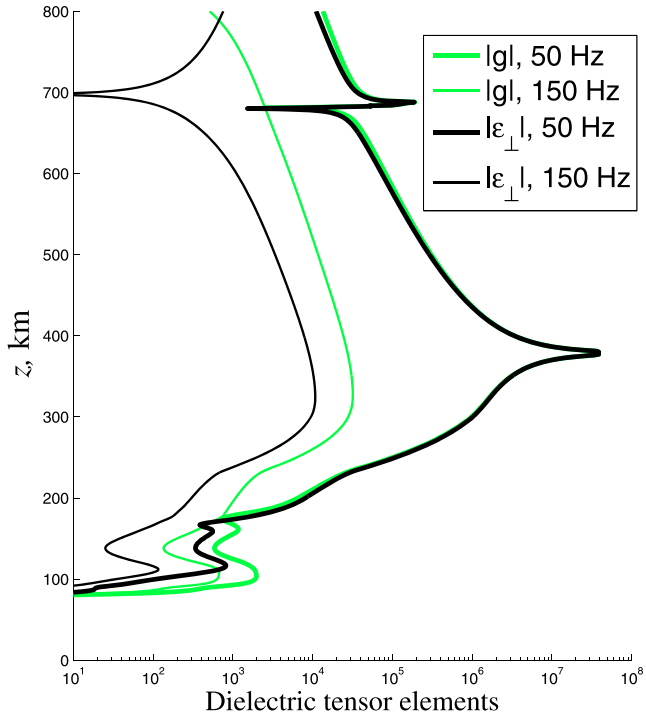

Figure 1. The vertical profile of absolute magnitudes of the dielectric tensor elements $\varepsilon_\perp(z)$ (black lines) and $g(z)$ (green lines) for f= 50 Hz (thick lines) and 150 Hz (thin lines) in the nighttime ionosphere.

$$\mathbf{B}_\tau = \overline{\mathbf{Y}}_\infty \mathbf{e}_\tau. \tag{7}$$

This condition assumes that in the upper ionosphere the excited electromagnetic field is a combination of outgoing waves $\propto \exp(+ik_z z)$. The field-aligned wave vector k_z and the matrix $\overline{\mathbf{Y}}_\infty$ can be found from the local dispersion equation in the Appendix B.

2.3. Admittance Method to Calculate the Electromagnetic Field at Arbitrary Altitude

Our numerical calculation scheme is based on the introduction of the admittance matrix $\overline{\mathbf{Y}}(z)$, that is, 2×2 matrix connecting horizontal components of electric and magnetic perturbations $\mathbf{B}_\tau = \overline{\mathbf{Y}}\mathbf{e}_\tau$. The admittance matrix $\overline{\mathbf{Y}}(z)$ obeys the generalized Riccati equation (Budden, 1966)

$$\partial_z \overline{\mathbf{Y}} = -\overline{\mathbf{Y}}\mathbf{T}^{eb}\overline{\mathbf{Y}} + \mathbf{T}^{be}, \tag{8}$$

which follows from the homogeneous system corresponding to the basic system (4) (for details see, e.g., Fedorov et al., 2016). In accordance to the boundary conditions for the horizontal components of electromagnetic field (see subsection 2.2), the boundary conditions for the admittance matrix are as follows: $\overline{\mathbf{Y}} = \overline{\mathbf{Y}}_g$ at $z=0$, and $\overline{\mathbf{Y}} = \mathbf{Y}_\infty$ at $z\to\infty$ (in reality the altitude z = 2,000 km was adopted as the upper boundary). Solving numerically the Cauchi problem with the boundary value $\overline{\mathbf{Y}}_g$ upward from the ground level ($z=0$), we get the admittance matrix at all altitudes below the source ($z<h$): $\overline{\mathbf{Y}}(z) = \overline{\mathbf{Y}}_-(z)$. In a similar way, the numerical solution of the Cauchi problem from $z=\infty$ gives us the admittance matrix profile above the source: $\overline{\mathbf{Y}}(z) = \overline{\mathbf{Y}}_+(z)$.

Let us return to the solution of the Maxwell's system (4). At the level of driving current ($z=h$) the matching condition must be fulfilled: the horizontal component of the electric field is to be continuous, whereas the magnetic component has a discontinuity as follows:

$$\mathbf{e}_\tau(h+0) - \mathbf{e}_\tau(h-0) = 0, \qquad \mathbf{B}_\tau(h+0) - \mathbf{B}_\tau(h-0) = (2\pi)^{-1}\mu_0 J_0 \hat{\mathbf{x}}. \tag{9}$$

The condition (9) is obtained by the integration of Equation 4 through the source level, that is, from h−0 to h+0. The magnetic field ump $\mathbf{B}_\tau(h+0) - \mathbf{B}_\tau(h-0)$ is thus proportional to the driver current intensity J_0. From the condition (9) it follows that

$$\mathbf{e}_\tau(h) = (2\pi)^{-1}\mu_0 J_0 \left[\overline{\mathbf{Y}}_+(h{+}0) - \overline{\mathbf{Y}}_-(h{-}0)\right]^{-1}\hat{\mathbf{x}}, \qquad \mathbf{B}_\tau(h\pm0) = \overline{\mathbf{Y}}_\pm(h\pm0)\mathbf{e}_\tau(h).$$

Starting from these values as the boundary conditions we solve numerically the Cauchi problems for the Maxwell's equations (4) upward and downward from the source level $z=h$. This way the horizontal components of the electromagnetic field $\mathbf{e}_\tau(z)$ and $\mathbf{B}_\tau(z)$ are found at any altitude.

The advantage of the admittance approach is that it enables one to avoid numerical instabilities caused by growing exponential solutions. The stability of the numerical solution is significantly improved by step-by-step corrections using the precomputed admittance matrix $\overline{\mathbf{Y}}(z)$. The system (4) has been numerically solved using the Runge-Kutta method. For the Fourier transform (2.1) the asymptotics of the spatial harmonics $\mathbf{B}(k_x)$ and $\mathbf{e}(k_x)$ has been used as described in the Appendix A.

3. Parameters of the Medium and Source

Height dependence of the components of the dielectric permeability tensor (2) has been calculated using the International Reference Ionosphere (IRI) model for charged particles and the Mass-Spectrometer-Incoherent-Scatter (MSIS) model for neutrals (Figure 1). The tensor elements $\varepsilon_\perp$ and g determine the

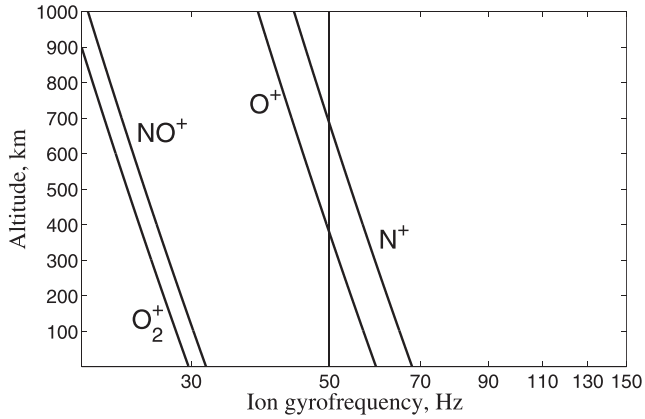

Figure 2. The vertical profile of gyrofrequencies $f_j(z)=\Omega_j(z)/2\pi$ of various ionospheric ions.

refraction indices of possible wave modes, which are considered in section 4 and Appendix B. The vertical profile of the tensor elements $\varepsilon_\perp(z)$ and g demonstrates resonance signatures at altitudes that correspond to 50 Hz O^+ ion gyrofrequency near 375 km and the N^+ ion gyrofrequency near 680 km. Figure 2 shows the altitude distribution of cyclotron frequencies $2\pi\Omega_j(z)$ for all ionospheric ions. The strong variation of tensor element $\varepsilon_\perp(z)$ (especially evident in log-scale) for $f=150$ Hz at $z\simeq 700$ km (accidentally near the N^+ resonance at 50 Hz) is not due to ion resonance but corresponds to the area where the magnitude of $|\varepsilon_\perp(z)|$ strongly diminishes, namely, $\mathrm{Re},\varepsilon_\perp(z)$ goes through 0, whereas $\mathrm{Im},\varepsilon_\perp(z)\neq 0$ while being very small. The occurrence of this region exerts no influence on the wave refraction index at 150 Hz (see section 4).

The IRI parameters have been chosen to correspond to nighttime/daytime conditions (LT = 00/12) at geographic latitude 69°N and longitude 34°E. The field inclination at this latitude is $I=78°$. However, for simplicity we suppose that geomagnetic field is vertical $I=90°$. The input IRI parameters—day, year, and latitude—have been chosen rather arbitrarily, because for any other parameters the results would be qualitatively the same. The ionospheric conditions correspond to the IRI-derived static Pedersen and Hall nighttime/daytime conductances $\Sigma_P=0.21/1.44$ S, $\Sigma_H=0.22/1.68$ S; and F layer peak heights hmF2 = 336/352 km. The power line is supposed to be suspended at height $h=5$ m. Ground resistance was chosen to be between 10^2 and 10^5 Ohm·m. The conductivity of the atmosphere is assumed to vary exponentially with altitude from the near-surface value $\sigma_a=1.1\cdot 10^{-14}$ S/m to merge the value at $z=80$ km predicted by the IRI model.

The appearance of the resonance pole and zero of the wave refraction index with an opaque band between them is a characteristic feature of multi-ion plasma (e.g., Mikhailova et al., 2012). However, the collisional effects may smear the opaque region in multicomponent plasma. In the ion resonance region, the coefficients of Maxwell's equations experience rapid variations, which may result in an insufficient accuracy of their interpolation. This difficulty was overcome by using linear interpolation of inverse elements of the tensor in the altitude range in the vicinity of cyclotron resonance. This approach provides a high accuracy of the differential equation solution. The ion resonance takes place for the heavily damping mode (see section 4), so the occurrence of such region does not influence noticeably the total wave energy transmission through the ionosphere.

The modeling results will be provided for the current intensity $J_0=1$ A. As a first step, we suppose the line current is infinitely long. Therefore, we set $k_y=0$ in Equation 4. This assumption will overestimate somewhat the ionospheric effect from realistic power lines with a finite length L.

4. ELF Modes in the Ionosphere

The dispersion equation (B1) describes two modes with left-hand (LH) and right-hand (RH) circular polarization in the geometric optic approximation. The complex value $k_z=\mathrm{Re}\,k_z+i\mathrm{Im}\,k_z$ enables one to estimate local propagation and absorption properties of electromagnetic modes. In the RH circular polarized wave mode, the magnetic and electric field vectors **E** and **B** rotate clockwise, in the same direction as electrons looking along magnetic field $\mathbf{B}_0$. In the LH polarized mode, the vectors **E** and **B** rotate anticlockwise similar to ions in field $\mathbf{B}_0$.

The altitude variations of $k_z(z)$ for both wave modes at 50 Hz and its harmonic at 150 Hz in the ionosphere are shown in Figure 3 for nighttime conditions. The $\mathrm{Re}\,k_z(z)$ is proportional to the wave refraction index $n=\mathrm{Re}\,k_z/k_0$ (Figure 3, upper panel). The damping rates $\propto\mathrm{Im}\,k_z(z)$ for the RH and LH emissions are shown in Figure 3, bottom panel. This plot evidences that damping rate of the emission with LH polarization is several orders of magnitude larger than that with RH polarization. The resonant-like features of the LH mode near 375 and 680 km are caused by the resonance with O^+ and N^+ ions. Therefore, in the upper ionosphere in the frequency band under consideration only a mode with RH polarization can be observed.

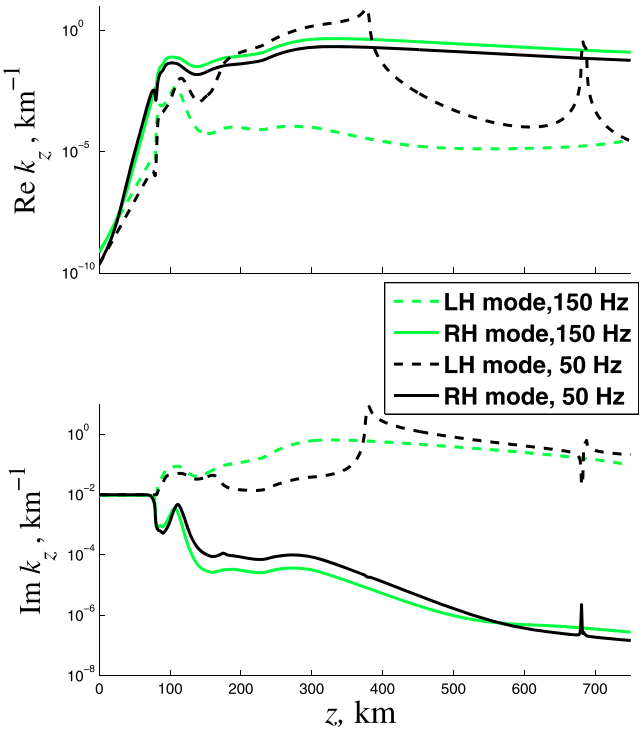

Figure 3. The local propagation and absorption properties of the electromagnetic 50 Hz (black lines) and 150 Hz (green lines) emissions in the RH and LH polarized modes: the vertical profile of the wave number Re k_z (top panel), and the damping rate Im k_z (bottom panel). Ionospheric parameters correspond to 28 November 2004, nighttime (21 UT), and k_x=10^{-2} km^{-1}.

This consideration interprets the transformation of the linear-polarized signal on the ground produced by a line current into circular polarized emission in the ionosphere. Linear-polarized disturbance can be decomposed into two circular polarized RH and LH modes. Both modes attenuate in a similar way in the atmosphere with scale ∼100 km owing to geometric spreading (Figure 3). Above 75–80 km, the RH mode attenuation suddenly drops because this mode is partially guided by the geomagnetic field. At the same time, the attenuation of nonguided LH mode increases. The corresponding penetration depth for RH mode in the *E* layer varies from several hundred to thousand km. Above the E-layer the partially guided RH mode propagates upward practically without attenuation with scale ∼10^4 km. The nonguided LH mode decay scale is ∼20 km above ∼90 km. As a result, the LH mode practically disappears up to upper part of the *E* layer (∼150 km).

5. Generation of Power Line Harmonics

Phase and amplitude disbalances of voltage and current may occur in power transmission lines, which result in power losses owing to electromagnetic energy radiation. An amount of global emitted energy has been ever increasing since the world total electric generation power increases. A sudden increase in PLHR events observed by LEO satellite was noticed in 2009, when extrahigh-voltage (EHV) and ultrahigh-voltage (UHV) transmission projects started to develop rapidly (Wu et al., 2019).

The appearance of power line current harmonics may be caused by the presence of thyristor power controllers in control circuits of large electricity consumers. The magnitudes of the currents in power lines in the favorable regime of the so-called natural power (when magnetic power equals electric power) in 220/330/500/750 kV lines are 315/612/1040/1620 A upon the transmitted active power 120/350/900/2100 MW, accordingly. Powerful industrial transformers are designed in such a way to have a working induction of the magnetic field in rods ∼1.6 T under nominal voltage, which are near the boundary of technical saturation of the electrotechnical steel. When the voltage exceeds the nominal magnitude under an impact of geomagnetically induced currents (GICs) a nonlinearity of magnetization of the electrotechnical steel happens, and this results in distortion of magnetization current and generation of higher harmonics in a power line. For example, 10% overvoltage causes a 2 times increase of the magnetization current as compared with the nominal value. In this case, the current holds harmonics of the basic 50/60 Hz current. Only odd harmonics are generated upon bipolar saturation regime, that is, the saturation of magnet core upon both positive and negative magnetic induction. The observations of PLE at DEMETER satellite indeed routinely detected intensity increases at odd harmonics of base power system frequencies, whereas even harmonics were generally absent (Nemec et al., 2015). The saturation of the magnet core of a power transformer and magnetization current may become unipolar, which occurs only for induction of one particular sign. In this case, the current's spectral content holds the entire spectrum of harmonics, both odd and even.

The appearance of harmonics is a signature of saturation of the magnetic system of a power transformer under an impact of GIC. The detection of PLE at a large distance from a three-phase power line is an indicator of its unbalanced operation.

According to the DEMETER multiyear observations, PLE intensity was increased at the times of higher GIC proxy values (Nemec et al., 2015). The GIC proxy at a given time was calculated from a ground magnetometer, which was the closest to the spacecraft location, as the maximum of dB/dt values over the 1 hr long time interval. The PLE intensities at the base power system frequency and its third harmonic in the European and U.S. regions observed during large GIC proxy values were systematically larger than the intensities observed during low GIC proxy. During the night, both the overall intensities and their variation as a function of the GIC proxy values were considerably larger than during the day.

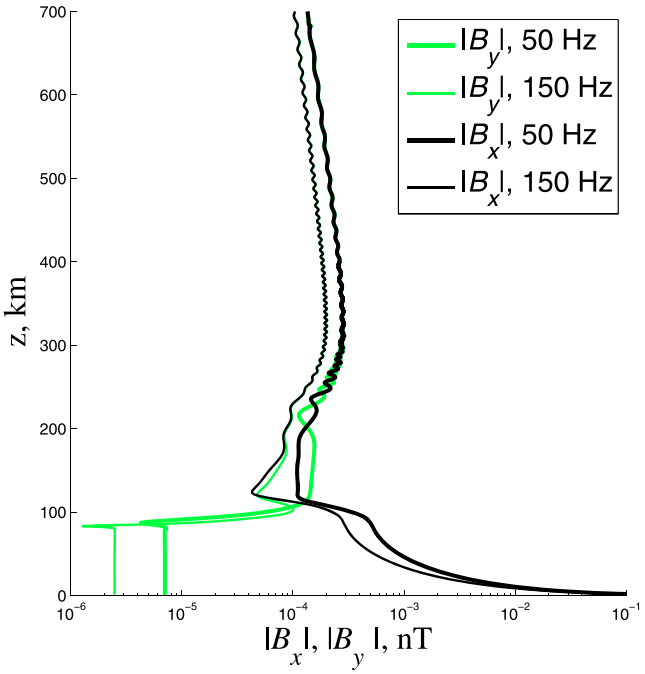

Figure 4. The altitudinal profile of the magnetic component magnitude $|B_x(z)|$ (black lines) and $|B_y(z)|$ (green lines) of electromagnetic emission generated by line current oscillating at f=50 Hz (thick lines) and 150 Hz (thin lines). The model parameters correspond to 28 November 2004, nighttime, and σ_g=10^{-4} S/m.

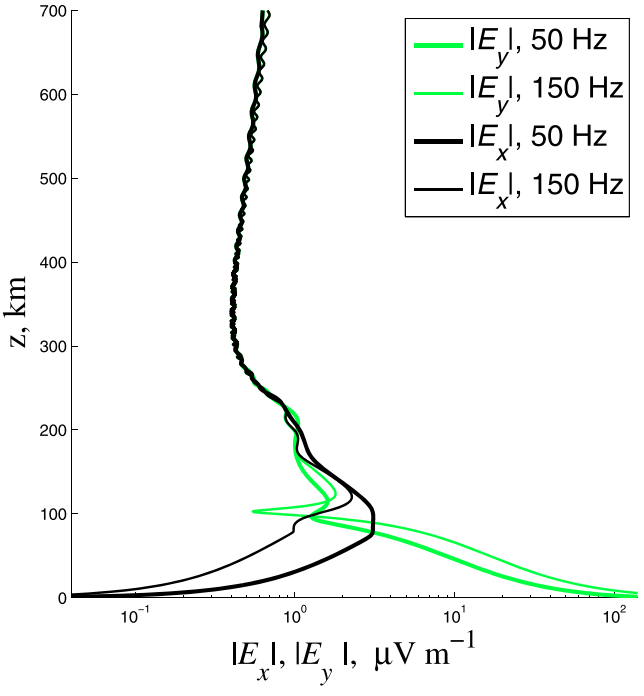

Figure 5. The altitudinal profile of the electric component magnitude $|E_x(z)|$ (black lines) and $|E_y|$ (green lines) of electromagnetic emission generated by line current at f = 50 Hz (thick line) and 150 Hz (thin line). The model parameters correspond to 28 November 2004, nighttime, and $\sigma_g = 10^{-4}$ S/m.

Further, we provide the modeling results for the fundamental frequency 50 Hz and its third 150 Hz harmonic to demonstrate their leakage features into the ionosphere.

6. Vertical Structure of Electromagnetic Field Generated by a Line Current

The vertical structure of the amplitude of magnetic components generated by 1 Ampere ground current at 50 and 150 Hz is shown in Figure 4 for nighttime conditions. In the upper ionosphere ($z \simeq 300-700$ km) above high-resistive crust ($\sigma_g = 10^{-4}$ S/m) the 50 Hz transverse magnetic field $|B_x(z)|$ and $|B_y(z)|$ can reach up to ~0.14–0.28 pT, depending on altitude. The 150 Hz harmonic has in the ionosphere the amplitude ~1.4 times less.

The vertical structure of the amplitude of transverse electric components $|E_x(z)|$ and $|E_y(z)|$ is shown in Figure 5. The electric field amplitudes in the upper nightside ionosphere produced by the same current with the frequency 50 Hz may reach up to ~0.4–0.7 μV/m. The 150 Hz harmonic has in the ionosphere nearly the same amplitude.

The nonmonotonic variation of the electromagnetic field amplitude with altitude is due to a nonmonotonic variation of the plasma refraction coefficient. In Figures 4 and 5, the field amplitudes above ~250 km show small-amplitude oscillations superimposed on the curves. These small oscillations are the result of a weak wave reflection from the region of the ion cyclotron resonance and formation of standing wave. Namely, the resonance with O^+, NO^+, and He^+ ions occur at altitudes about 375, 680, and 1,060 km. Above these resonance regions such periodic vertical structure is absent.

6.1. Comparison of Main Frequency and Harmonic

Apart from the vertical structure of the amplitude of magnetic and electric components at 50 Hz, Figures 4 and 5 show the structure of the electromagnetic field at 150 Hz harmonic for the same $J_0 = 1$ A. The amplitudes of 150 Hz emission in the ionosphere ($z \simeq 300$–700 km) is about the same as those at 50 Hz. At the same time, higher-order harmonics (200–1,000 Hz) penetrate through the ionosphere better than fundamental 50/60 Hz and its lower harmonics, ≤150 Hz (not shown).

However, in the atmosphere at low altitudes the electric field at harmonic frequency is larger than that at the main frequency (Figure 5). Indeed, from the impedance condition (5) with $k_y = 0$ in the matrix (6) it follows that at the Earth's surface the electric and magnetic components e_y and B_x are coupled by the relationship $e_y = \overline{Z}_g(H)B_x$, where $\overline{Z}_g(H)(\omega)$ is the normalized ground impedance of magnetic mode

$$\overline{Z}_g(H) = [\overline{Y}_g^{(H)}]^{-1} = k_0\left(i\omega\mu_0\sigma_g - k_x^2\right)^{-1/2}.$$

If the main contribution into the electromagnetic field is provided by large horizontal scales ($k_x\delta_g \ll 1$, where $\delta_g = (\omega\mu_0\sigma_g)^{-1/2}$ is the skin depth), the relationship for the electric field reduces to

$$e_y(\omega) \simeq \exp(-i\pi/4)\sqrt{\omega\varepsilon_0/\sigma_g}\, B_x(\omega). \quad (10)$$

Because in a near-field zone magnetic field is weakly dependent on ω, the electric field, as follows from Equation 10, increases with an increase of frequency, $e_y(\omega) \propto \omega^{1/2}$. In the case of small horizontal scales, the surface

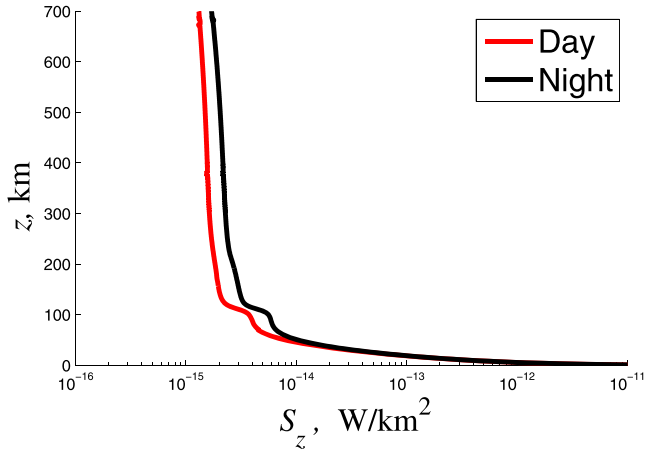

Figure 6. The altitudinal distribution of Poynting wave energy flux density S_z generated by near-Earth oscillating 50 Hz line current in the nighttime (black line) and daytime (red line) ionospheres.

impedance is $Z_g^{(H)} \propto \omega$, so the electric field $e_y(\omega) \propto \omega$. This consideration explains the growth of harmonic amplitude in the bottom atmosphere with frequency.

6.2. Comparison of Day/Night Transmission

For a qualitative comparison of the ELF transmission through the daytime and nighttime ionosphere, we compare modeling results for the nighttime (00 LT = 21 UT) and daytime (12 LT = 09 UT) conditions. Figure 6 shows the superposed altitudinal distributions of the Poynting flux S_z of the electromagnetic wave energy at 50 Hz for dayside and nighttime conditions. According to the modeling results, the penetration through the ionosphere during nighttime is more efficient than during daytime, though the difference is not very large. At 660 km during night hours the Poynting flux is about 35% larger than during daytime.

6.3. Comparison of High-/Low-Resistive Crust

The intensity of electromagnetic emission by a power line strongly depends on the resistivity of the underlaying crust. Figure 7 shows comparison of the vertical Poynting flux density S_z of electromagnetic emission for two extreme cases: the emitter above a high-resistive ($\sigma_g = 10^{-5}$ S/m) and low-resistive ($\sigma_g = 10^{-2}$ S/m) ground. The largest decrease of $S_z(z)$ occurs in the atmosphere (<100 km) owing to isotropic divergence of electromagnetic energy. Throughout the ionosphere the electromagnetic disturbance propagates upward with just a weak attenuation. This comparison shows that above a high-resistive crust the upward flux into the upper ionosphere is nearly 3 orders of magnitude larger than above a low-resistive crust, namely, at $z = 450$ km $S_z = 3.2 \cdot 10^{-18}$ W/km^2 under $\sigma_g = 10^{-2}$ S/m, whereas $S_z = 2.1 \cdot 10^{-15}$ W/km^2 under $\sigma_g = 10^{-5}$ S/m.

In Figure 8 we compare the electric component magnitudes $|E_x(z)|$ and $|E_y|(z)$ in the nighttime ionosphere excited by the line current at 50 Hz above the crust with conductivities $\sigma_g = 10^{-2}$ S/m and $\sigma_g = 10^{-4}$ S/m. The increase of ground conductivity σ_g by 2 orders of magnitude from 10^{-4} S/m up to 10^{-2} S/m results in about order of magnitude decrease of excited electric field in the upper ionosphere ($z = 600$ km), from ~0.57 to ~0.06 μV/m.

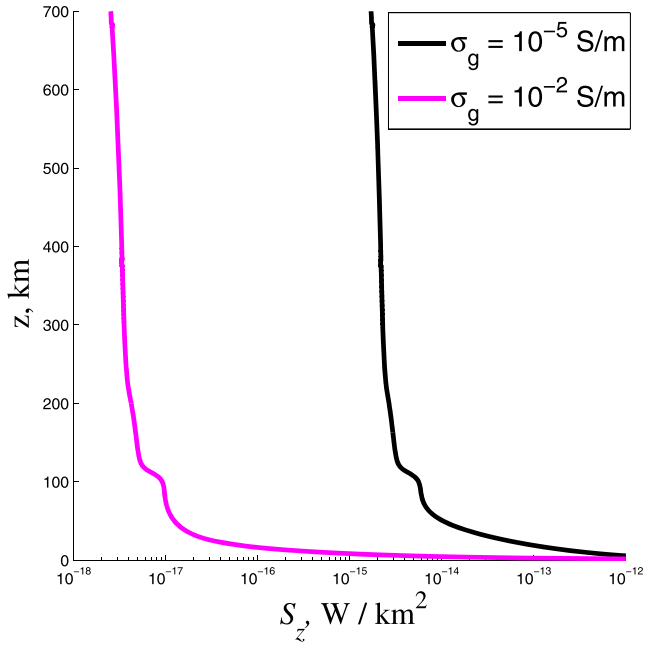

Figure 7. The altitudinal distribution of Poynting energy flux S_z generated by near-Earth oscillating 50 Hz line current above a high-resistive (σ_g=10^{-5} S/m) and low-resistive (σ_g=10^{-2} S/m) crust during nighttime.

In a qualitative way, the electromagnetic field induced by current flowing in an infinitely long conductor at height h above the ground would arise from this current and opposite image current at depth $\sqrt{2}\delta_g(\sigma, \omega)$ (Yearby et al., 1983). For a high ground conductivity, the image current tends to cancel partially the field produced by the main linear current.

7. Discussion

The number of PLE observations in space with measured amplitudes is not very large. The LEO microsatellite Chibis-M with the electrical sensor with the base of 0.4 m for measurements in the frequency range of 0.1 – 40,000 Hz, obtained a large volume of observational data on PLE (Korepanov et al., 2015; Dudkin et al., 2015). For example, during each passage over the high voltage power lines in Brazil an enhancement of the amplitude of the band-filtered electric signal at 60 Hz up to $E \simeq 0.6$–1.0 μV/m and spectral power up to $W_E \simeq 0.7$ (μV/m)^2/Hz were recorded. According to the modeling results (Figure 5) PLE with intensity ~1 μV/m can be produced by ~2 A unbalanced current above a high-resistive crust ($\sigma_g = 10^{-4}$ S/m). If a power line is located above a low-resistive crust (e.g., $\sigma_g = 10^{-2}$ S/m), for the same emission intensity the unbalanced current must be ~20 A.

In the study by Zhang and Ma (2018), during 6.5 operating years of DEMETER satellite 133 PLHR events with frequencies from 500 Hz to

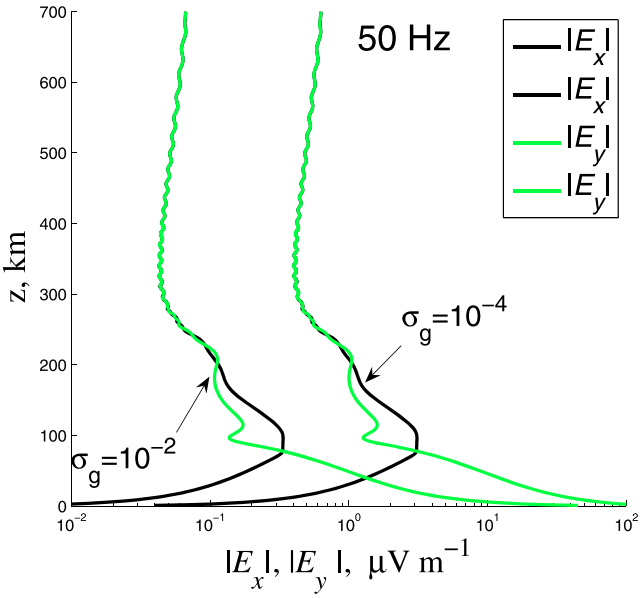

Figure 8. The altitudinal profile of electric component magnitudes $|E_x(z)|$ (black lines) and $|E_y(z)|$ (green lines) of electromagnetic radiation generated by line current at $f = 50$ Hz above the crust with conductivities $\sigma_g = 10^{-2}$ S/m and $\sigma_g = 10^{-4}$ S/m. The ionospheric parameters correspond to 28 November 2004, nighttime.

4.5 kHz were detected in the near-Earth space above China. Nearly all the PLHR events had corresponding PLEs at the fundamental 50 Hz frequency of local power system. Moreover, PLEs were even more detectable than PLHRs. Weak 60 Hz PLE were often detected above the east coast of China, which suggested the propagation from western Japan. Power spectral density of PLE electric field fluctuations was up to $W_E \sim 0.1\,(\mu V/m)^2/Hz$, which corresponds to electric field intensity $E \simeq \sqrt{W_E \Delta f} \simeq 0.6\,\mu V/m$ in the band $\Delta f = 4$ Hz. According to our modeling results (Figures 5 and 8), such intensities in the nighttime upper ionosphere are expected for the unbalanced current intensity ~1–10 A, depending on the crust resistivity. Thus, unbalanced currents in a power line with intensities of about units tens of amperes are capable of producing PLE with amplitude sufficient to be detected by electric sensors of LEO satellite. The magnetic component of PLE even under the same favorable case of high ground resistivity is to be ~0.1 pT for $J_0 = 1$ A. Such signal may be hidden by interference and background noise.

The geographic maps of the occurrence rates of 50/60 Hz emissions recorded by DEMETER satellite showed remarkable agreement with the world map of power consumption and the base power system frequency (Nemec et al., 2015). This demonstrated that above industrialized areas the PLE intensity is significantly enhanced above normal levels. It should be noted that 50/60 Hz increases were not observed above geomagnetically conjugate points, suggesting that the effects of PLE are limited primarily to the hemisphere of origin. The median power spectral densities W_E of PLE in the European and U.S. regions range from tenths to units of $(\mu V/m)^2\,Hz^{-1}$. They are generally larger during the night than during the day (Nemec et al., 2008). As section 6.2has shown this is likely related to the wave attenuation during the propagation through the ionosphere.

The estimate of the unbalanced current necessary for the PLE/PLHR detection was made by Wu et al. (2019) on the basis of the following assumptions. The formula for the power radiated into a free space by a small oscillating magnetic dipole from Yearby et al. (1983) was used. The magnetic dipole is formed by a line current and its image ground return current. The radiated power should exceed the threshold 0.5 W necessary to trigger magnetospheric VLF emissions according to satellite observations. From the latter condition the minimum unbalanced current was estimated. For 110 kV power line the estimated unbalanced current at 50 Hz was $J_0 \simeq (2–6)\cdot 10^3$ A, which is much larger than predicted by our numerical model. We suppose that consideration used in Wu et al. (2019) may be applied for simple estimate in the PLHR frequency range (around 1 kHz), but not in the PLE range (50/60 Hz).

In the model presented here, several simplifications have been made. They will not modify the results considerably, but, nonetheless, further modeling efforts are needed to account for a finite inclination of the geomagnetic field, lower latitudes, and a finite length of the line current L. The account for a finite L will somewhat decrease the ionospheric response to a ground power line. Nonetheless, despite some simplifications, the model presented here is more adequate and precise than the preceding models.

Man-made electromagnetic pollutants of the near-Earth space, PLHR and PLE, may interact with particles and natural waves, causing wave growths, triggering natural emissions and electron precipitations, and altering the state of the ionosphere (Bullough et al., 1985). The significance of the power line emission will continue to increase with the growth of global industry (even now PLHR intensities are ~10 dB stronger than the background noise), so these effects merit further studies.

8. Conclusions

We have modeled the penetration of ELF emission into the realistic ionosphere from a ground source modeled as an infinite line 50–150 Hz current. The upward flux into the upper ionosphere of electromagnetic emission by the near-ground power line strongly depends on the ionospheric density and resistivity of the

underlaying crust. During nighttime hours and above a high-resistive crust it is substantially larger. The modeling shows that ELF signals from such source with unbalanced current intensity about several units tens of amperes (depending on the crust resistivity) can be reliably detected by an electric sensor onboard a LEO satellite.

Appendix A: Asymptotics of the Atmospheric Solution for Small Wave Scales

The numerical scheme of the exact solution of the system (4) by Runge-Kutta method upon growth of parameter k_x (small scales) becomes unstable. Upon decrease of the altitude z, the function $B_x(k_x)$ decays more slowly, and at $z=0$ it even tends to a finite limiting value at $k_x\to\infty$. To calculate effectively the Fourier transform over k_x, we have used the asymptotics of the exact solution at $k_x\to\infty$.

For the components e_x and B_y at all altitudes, and for the components B_x and e_y at high altitudes, it is sufficient just to extrapolate the solution with the decaying exponential function of k_x. At low altitudes (tens of kilometers and less) the situation becomes more complicated. However, in this region the asymptotic analytical solutions can be used. Neglecting the Hall conductivity, the system (4) takes the form

$$\partial_z B_x = -i\frac{\kappa_a^2}{k_0}e_y,\ \partial_z e_y = -ik_0 B_x, \tag{A1}$$

where $\kappa_a=(k_0^2\varepsilon_a-k_x^2)^{1/2}$ is a vertical wave number in the atmosphere and $\varepsilon_a=1+i\sigma_a(\omega\varepsilon_0)^{-1}$ is the complex dielectric permittivity of the atmosphere. To find asymptotics, we use the system (A1), assuming that its coefficients are weakly altitude dependent. The validity of this assumption will be given further. The solution of this system that satisfies the boundary condition at the Earth's surface (5) has the form

$$B_x = B_1\left(e^{-i\kappa_a z}+R_g e^{i\kappa_a z}\right),\qquad e_y=\frac{k_0}{\kappa_a}B_1\left(e^{-i\kappa_a z}-R_g e^{i\kappa_a z}\right),$$

where the Earth reflection coefficient is $R_g=(\kappa_g-\kappa_a)(\kappa_g+\kappa_a)^{-1}$, $\kappa_g=(k_0^2\varepsilon_g-k_x^2)^{1/2}$. On the other hand, the solution with the emission condition (7) at $z\to\infty$ can be written as

$$B_x = B_2 e^{i\kappa_a(z-h)},\qquad e_y=-\frac{k_0}{\kappa_a}B_2 e^{i\kappa_a(z-h)}. \tag{A2}$$

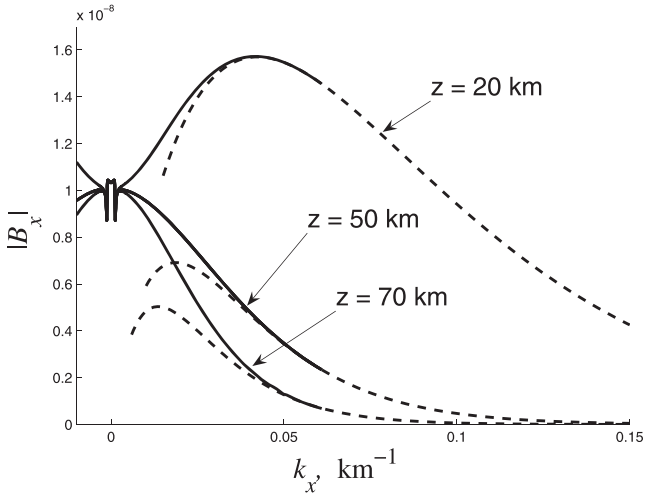

Figure A1. Spectral structure of disturbance $|B_x(k_x)|$ resulted from the numerical calculations (solid lines) and from the asymptotic formulas (dashed lines) at various altitudes.

The coefficients B_1 and B_2 are to be found using the matching condition (9) at the level of driving current $z=h$. This way we obtain the linear system, which solution is

$$B_1 = -(4\pi)^{-1}\mu_0 J_0 e^{i\kappa_a h},\qquad B_2=(4\pi)^{-1}\mu_0 J_0\left(1-R_g e^{2i\kappa_a h}\right).$$

The simple formulae (A2) may be used under the condition $|k_x|\gg|k_0\varepsilon_a^{1/2}|$, which is the condition for the coefficients of the system (A1) to be constant, because $\kappa_a\approx ik_x$. If this condition holds till some altitude z_*, then at $z<z_*$ the amplitudes $|B_x|$ and $|e_y|$ behave $\propto\exp(-k_x z)$. If, besides that $k_x\gg z_*^{-1}$, then waves reflected from layers $z>z_*$ are exponentially small and can be neglected. In this range of wave numbers the approximation (A2) is valid with $\kappa_a=ik_x$.

Numerical calculations have proven that at $z<70$ km the components $B_x(k_x)$ and $e_y(k_x)$, obtained from the solution of a complete system (4) and calculated from the asymptotic formulae (A2) coincide with a good accuracy in a wide range of k_x (Figure A1).

Appendix B: Local Wave Numbers of the ELF Modes in the Ionosphere

Assuming that electromagnetic field in the ionosphere can be described in the Wentzel-Kramers-Brillouin (WKB) approximation $\propto \exp(i\int^z k_z(z')dz' + ik_x x)$ the local dispersion equation can be obtained from the basic system (4). For the case of $I = \pm 90°$ and $k_y = 0$ the dispersion equation has the form

$$k_z^4 + Bk_z^2 + C = 0,$$

where

$$B = \beta k_x^2 - 2k_0^2\varepsilon_\perp,\ \beta = 1 + \varepsilon_\perp/\varepsilon_\parallel,$$
$$C = k_0^4\left(\varepsilon_\perp^2 - g^2\right) - k_0^2k_x^2(\beta\varepsilon_\perp - g^2/\varepsilon_\parallel) + k_x^4(\varepsilon_\perp/\varepsilon_\parallel).$$

For a fixed k_x, the local value of k_z can be found from this biquadratic equation as

$$k_z^2 = k_0^2\varepsilon_\perp - 0.5\left[(1 + \varepsilon_\perp/\varepsilon_\parallel)k_x^2 \pm \sqrt{(1-\varepsilon_\perp/\varepsilon_\parallel)^2k_x^4 + 4\left(k_0^4g^2 - k_0^2g^2k_x^2/\varepsilon_\parallel\right)}\right]. \quad \text{(B1)}$$

The complex value $k_z = \mathrm{Re}\,k_z + i\mathrm{Im}\,k_z$ enables one to estimate local propagation and absorption properties of the electromagnetic modes. The Equation B1 describes two modes with LH (corresponding to the upper sign) and RH (corresponding to the lower sign) circular polarizations.

The main input into the electromagnetic field at ionospheric altitudes is provided by spatial harmonics with $k_x \sim 10^{-2}\,\mathrm{km}^{-1}$. At $f = 50$ Hz at altitudes greater than ~100 km the following inequalities hold: $k_0^2|g| > k_0^2|\varepsilon_\perp| \gg k_x^2$ and $|\varepsilon_\perp/\varepsilon_\parallel| \ll 1$. Therefore, the expression (B1) may be simplified by neglecting k_x and $|\varepsilon_\perp/\varepsilon_\parallel|$ as follows: $k_z^2 = k_0^2(\varepsilon_\perp \mp g)$. In the upper collisionless ionosphere, the relation (B1) is reduced to the following one (supposing for simplicity one sort of ions):

$$k_z^2 = k_0^2\left(1 - \frac{\omega_{pe}^2}{\omega(\omega \mp \Omega_e)} - \frac{\omega_{pi}^2}{\omega(\omega \pm \Omega_i)}\right). \quad \text{(B2)}$$

The physical insight into the wave absorption properties may be achieved by considering a plasma with one sort of ions. The field-aligned wave number k_z of the RH polarized mode has a singularity (resonance) at $\omega = \Omega_e$. This wave mode can propagate in the frequency range $0 < \omega < \Omega_e$, and in the MHD limit $\omega < \Omega_i$ it transfers into the fast magnetosonic wave. The LH polarized mode corresponding to the lower sign in (B2) has a singularity/resonance at $\omega = \Omega_i$, and in the MHD limit it transfers into the Alfvén mode. At frequencies $\Omega_i < \omega < \omega_0^{(3)}$ this mode becomes evanescent (nonpropagating), that is, $k_z^2 < 0$. The cutoff frequency $\omega_0^{(3)}$ may be estimated as follows: $\omega_0^{(3)} = \sqrt{\omega_{pe}^2 + 1/4\Omega_e^2} - 1/2\Omega_e$. A severe damping of the LH polarized mode in the ionosphere is mainly caused by the occurrence of opaque nonpropagating region for this mode. Natural electromagnetic emissions in this band (e.g., ion whistlers, $\omega < \Omega_i$) have RH polarization.

Data Availability Statement

The numerical model incorporates the vertical profiles of the ionospheric parameters derived from the International Reference Ionosphere (IRI) model (http://irimodel.org).

Acknowledgments

This research was supported by Grant 16-17-00121 from the Russian Science Foundation. We appreciate a very thorough examination of our paper by both reviewers.

References

Ando, Y., Hayakawa, M., & Molchanov, O. A. (2002). Theoretical analysis on the penetration of power line harmonic radiation into the ionosphere. *Radio Science*, *37*, 1093. https://doi.org/10.1029/2001RS002486

Barnett, P. S. (1974). The analysis of travelling waves on power system transmission lines (PhD Thesis), University of Canterbury, New Zealand, 359 p.

Bewley, L. V. (1942). Traveling waves on electric power systems. *Bulletin American Mathematical Society*, *48*, 527–538.

Budden, K. G. (1966). *Radio wave in the ionosphere* (p. 542). Cambridge University Press.

Bullough, K., Kaiser, R., & Strangeways, H. J. (1985). Unintentional man-made modification effects in the magnetosphere. *Journal Atmospheric and Terrestrial Physics*, *47*, 1211–1223.

Dudkin, F., Korepanov, V., Dudkin, D., Pilipenko, V., Pronenko, V., & Klimov, S. (2015). Electric field of the power terrestrial sources observed by microsatellite Chibis-M in the Earth's ionosphere in frequency range 1–60 Hz. *Geophysical Research Letters*, *42*, 5686–5693. https://doi.org/10.1002/2015GL064595

Fedorov, E., Mazur, N., Pilipenko, V., & Baddeley, L. (2016). Modeling the high-latitude ground response to the excitation of the ionospheric MHD modes by atmospheric electric discharge. *Journal Geophysical Research: Space Physics*, *121*, 11,282–11,301. https://doi.org/10.1002/2016JA023354

Helliwell, R. A., Katsurakis, J. P., Bel, T. F., & Raghuram, R. (1975). VLF line radiation in the Earth's magnetosphere and its association with power system radiation. *Journal Geophysical Research*, *80*, 4249–4258.

Koloskov, A. V., & Yampolski, Y. M. (2009). Observations of radiation from North American power mains in Antarctica. *Radiophysics and Radioastronomy*, *14*, 367–376.

Korepanov, V. E., Dudkin, F. L., & Pronenko, V. A. (2015). Observations of radiation from power lines in near-Earth space. *Geomagnetism Aeronomy*, *55*, 706–711.

Kostrov, A. V., Gushchin, M. E., & Strikovskii, A. V. (2017). Generation and radiation of high power line harmonics. *Geomagnetism Aeronomy*, *57*, 482–490. https://doi.org/10.1134/S0016793217030094

Luette, J., Park, C., & Helliwell, R. (1979). The control of the magnetosphere by power line radiation. *Journal Geophysical Research*, *84*, 2657–2660. https://doi.org/10.1029/JA084iA06p02657

Mazur, N. G., Fedorov, E. N., Pilipenko, V. A., & Vakhnina, V. V. (2018). ULF electromagnetic field in the upper ionosphere excited by lightning. *Journal Geophysical Research: Space Physics*, *123*, 6692–6702. https://doi.org/10.1029/2018JA025622

Mikhailova, O. S., Klimushkin, D. Y., & Mager, P. N. (2012). Pc1-pulsations: The parallel structure in the magnetosphere plasma with admixture of the heavy ions. *Advances in Astronomy and Space Physics*, *2*, 88–90.

Nemec, F., Parrot, M., & Santolik, O. (2015). Power line harmonic radiation observed by the DEMETER spacecraft at 50/60 Hz and low harmonics. *Journal Geophysical Research: Space Physycs*, *120*, 8954–8967. https://doi.org/10.1002/2015JA021682

Nemec, F., Santolik, O., Parrot, M., & Berthelier, J. J. (2006). Power line harmonic radiation (PLHR) observed by the DEMETER spacecraft. *Journal Geophysical Research*, *111*, A04308. https://doi.org/10.1029/2005JA011480

Nemec, F., Santolik, O., Parrot, M., & Bortnik, J. (2008). Power line harmonic radiation observed by satellite: Properties and propagation through the ionosphere. *Journal Geophysical Research*, *113*, A08317. https://doi.org/10.1029/2008JA013184

Park, C. G., & Helliwell, R. A. (1981). Power line radiation in the magnetosphere. *Advances Space Research*, *1*, 423–437.

Pfaff, R., Freudenreich, H., Simoes, F., & Liebrecht, C. (2014). *Observations of 50/60 Hz power line radiation in the low latitude ionosphere detected by the electric field instrument on the C/NOFS satellite*. Beijing, China: XXXI URSI General Assembly. https://doi.org/10.1109/URSIGASS.2014.6929584

Pilipenko, V. A., Parrot, M., Fedorov, E. N., & Mazur, N. G. (2019). Electromagnetic field in the upper ionosphere from ELF ground-based transmitter. *Journal Geophysical Research: Space Physics*, *124*, 8066–8080. https://doi.org/10.1029/2019JA026929

Rothkaehl, H., & Parrot, M. (2005). Electromagnetic emissions detected in the topside ionosphere related to the human activity. *Journal Atmospheric Solar-Terrestrial Physics*, *67*, 821–828.

Shprits, Y. Y., Subbotin, D. A., Meredith, N. P., & Elkington, S. R. (2008). Review of modeling of losses and sources of relativistic electrons in the outer radiation belt II: Local acceleration and loss. *Journal Atmospheric and Solar-Terrestrial Physics*, *70*, 1694–1713. https://doi.org/10.1016/j.jastp.2008.06.014

Simoes, F., Pfaff, R., Berthelier, J.-J., & Klenzing, J. (2012). A review of low frequency electromagnetic wave phenomena related to tropospheric-ionospheric coupling mechanisms. *Space Science Review*, *168*, 551–593.

Tatnall, A. R. L., Matthews, J. P., Bullough, K., & Kaiser, T. R. (1983). Power-line harmonic radiation and the electron slot. *Space Science Review*, *35*, 139–173.

Tomizawa, I., & Yoshino, T. (1985). Power line radiation observed by the satellite OHZORA. *Journal Geomagnetism Geoelectricity*, *37*, 309–327.

Wu, J., Fu, J. J., & Zhang, C. (2014). Propagation characteristics of power line harmonic radiation in the ionosphere. *Chinese Physics B*, *23*, 034,102–034,107. https://doi.org/10.1088/1674-1056/23/3/034102

Wu, J., Guo, Q., Yue, C., Xie, L., & Zhang, C. (2019). Special electromagnetic interference in the ionosphere directly correlated with power system. *IEEE Transactions on Electromagnetic Compatibility*, *62*, 947–954. https://doi.org/10.1109/TEMC.2019.2918280

Yearby, K. H., Smith, A. J., & Bullough, K. (1983). Power line harmonic radiation in Newfoundland. *Journal Atmospheric Solar-Terrestrial Physics*, *45*, 409–419. https://doi.org/10.1016/S0021-9169(83)81100-3

Zhang, C., & Ma, Q. (2018). Influences of radiation from terrestrial power sources on the ionosphere above China based on satellite observation. *2nd International Workshop on Renewable Energy and Development, Conference Series: Earth and Environmental Science*, *153*, 042002. https://doi.org/10.1088/1755-1315/153/4/042002